

Self-Assembly of Triton X-100 in Water Solutions: A Multiscale Simulation Study Linking Mesoscale to Atomistic Models

Antonio De Nicola,[†] Toshihiro Kawakatsu,[‡] Camillo Rosano,[§] Massimo Celino,^{||} Mattia Rocco,[§] and Giuseppe Milano^{*,†,⊥}

[†]Dipartimento di Chimica e Biologia, Università di Salerno, I-84084 via Ponte don Melillo, Salerno, Italy

[‡]Department of Physics, Tohoku University, Aoba, Aramaki, Aoba-ku, Sendai 980-8578, Japan

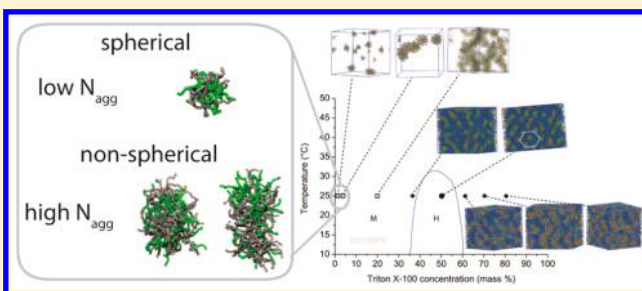
[§]Biopolimeri e Proteomica, IRCCS AOU San Martino-IST, Istituto Nazionale per la Ricerca sul Cancro, Largo R. Benzi 10 I-16132 Genova, Italy

^{||}ENEA, C.R. Casaccia, Via Anguillarese 301, I-00123 Roma, Italy

[⊥]IMAST S.c.a.r.l. Technological District in Polymer and Composite Engineering, P. leBovio 22, I-80133, Napoli, Italy

Supporting Information

ABSTRACT: A multiscale scheme is proposed and validated for Triton X-100 (TX-100), which is a detergent widely employed in biology. The hybrid particle field formulation of the model allows simulations of large-scale systems. The coarse-grained (CG) model, accurately validated in a wide range of concentrations, shows a critical micelle concentration, shape transition in isotropic micellar phase, and appearance of hexagonal ordered phase in the experimental ranges reported in the literature. The fine resolution of the proposed CG model allows one to obtain, by a suitable reverse mapping procedure, atomistic models of micellar assemblies and of the hexagonal phase. In particular, atomistic models of the micelles give structures in good agreement with experimental pair distance distribution functions and hydrodynamic measurements. The picture emerging by detailed analysis of simulated systems is quite complex. Polydisperse mixtures of spherical-, oblate-, and prolate-shaped aggregates have been found. The shape and the micelle behavior are mainly dictated by the aggregation number (N_{agg}). Micelles with low N_{agg} values (~ 40) are spherical, while those with high N_{agg} values (~ 140 or larger) are characterized by prolate ellipsoidal shapes. For intermediate N_{agg} values (~ 70), fluxional micelles alternating between oblate and prolate shapes are found. The proposed model opens the way to investigations of several mechanisms involving TX-100 assembly in protein and membrane biophysics.



INTRODUCTION

Detergents are widely employed in biology.^{1–9} As a prime example, they are used for the isolation of integral membrane proteins from biomembranes.^{1–5} Moreover, they are used in the crystallization of proteins, as membrane stabilizing, denaturing, permeabilizing agents, and for transfection.^{6–9} The tradename TritonX represents a class of nonionic surfactants whose basic units are composed of a hydrophobic aromatic 4-(1,1,3,3-tetramethylbutyl)-phenyl core and a hydrophilic, variable length poly(ethylene oxide) (PEO) chain, generally expressed as $C_{14}H_{22}O(C_2H_4O)_n$.¹⁰ This Triton X is ubiquitous for the aforementioned applications. In particular, Triton X-100 (TX-100), whose side chain has 9–10 PEO blocks, is a detergent molecule widely used in the biological sciences.⁴ A recent search for “Triton X-100” in the database PubMed¹¹ that we performed while writing the present paper recovered ~ 900 hits in the “Title” field and more than 13 800 hits in the combined “Title/Abstracts” fields. Currently, in the Protein Data Bank,¹² there are ~ 60 structures that contain TX-100 moieties. For instance, in the crystal structures for full-

length, glycosylated nonstructural protein 1 (NS1) from West Nile and dengue viruses, surfaces for associations with membranes have been revealed by using TX-100 and crystallizing the protein in the presence of this detergent.¹³ These structures provide a better molecular understanding of how these viruses approach and infect cells, and this is a key step toward virus control. Another recent example is the X-ray structure of a lipid-bound extended synaptotagmin (E-SYT2).¹⁴ In particular, E-SYT2 binds TX-100 as a lipid-like molecule in the hydrophobic channel of SMP domain (a lipid-binding module present in several proteins localized at membrane contact site). These structures are very relevant, because they provided evidence for a role of SMP-domain-containing proteins in the control of lipid transfer.

Many lower-resolution studies using small-angle X-ray or neutron scattering (SAXS/SANS) or hydrodynamics on the solution conformation of TX-100 solubilized proteins have

Received: May 23, 2015

Published: August 18, 2015



been reported.^{4,5,15} TX-100 is also an important molecule for the study of biomembrane microdomains. Because of the variety of the composition and the complexity of biomembranes, the use of detergents represents a way to separate and study membrane components.² These procedures can reveal insoluble fractions (called detergent-resistant membranes),¹ which are rich in raft-like components.^{3,5,15–21} At high surfactant concentrations, where hexagonal or bicontinuous phases are stable (35%–60% w/w), Triton assemblies are used as templates to obtain nanostructured and/or porous materials. In particular, mesoporous nanoparticles can be synthesized using TX-100 templating to improve sustained drug release and patterns with high drug loading.²² Conductive microemulsions for CoNi electrodeposition can be obtained using, as a templating agent, a bicontinuous aqueous solution–surfactant–oil system based on TX-100.²³ Generally, TX-100 is a very common soft templating agent in the synthesis of nanostructures.²⁴

Accurate and carefully validated molecular models of well-relaxed assembled structures of TX-100 at different water contents, going in water from low contents (where micellar assemblies are stable) to high contents of TX-100 (where bicontinuous or hexagonal phases are stable),^{25,26} would be highly desirable. Indeed, these structures would be a good starting point in relevant applications of molecular dynamics (MD) for protein, as for biomembranes, and for other systems relevant for the aforementioned applications.

However, to the best of our knowledge, only a few computational TX-100 models have been reported, such as the early atomistic study on the conformational behavior of a single TX-100 molecule in vacuum and in water.²⁷ Very recently, an optimized set of CHARMM parameters for the Triton X-series, suitable for atomistic molecular dynamics (MD) simulations, has been presented.²⁸ Although atomistic simulations provide very detailed models of surfactants, they are very computationally expensive techniques for studying the assembling processes involving nanostructures occurring on the mesoscopic time and length scales. Indeed, the assembly process of surfactants can be obtained only in some cases from a random mixture of surfactants in aqueous solution within atomic resolution with reasonable simulation time. Typically, this happens only for diluted systems above the CMC, and, more generally, in cases where the self-assembly occurs on a time scale that is attainable with atomistic simulations (100 ns).^{29–32} For this reason, in most cases, atomistic MD studies are conducted using preassembled aggregates. A systematic MD study of assembly process of micelles reported by Nevidimov et al.³³ has shown, as can be reasonably assumed, that random mixtures provide a lower dependence of final results on initial conditions, compared to the calculations using preassembled aggregates.

MD simulations of CG models allow one to observe the self-assembly process spontaneously.^{29,34–36} In particular, taking advantage of the large time scales accessible at the CG level, simulations on the order of 1–10 μ s allow to follow the self-assembly process and to efficiently sample different fluxional size and shapes characterizing assemblies of surfactants. For example, MD simulations of CG models allowed study of the assembly of various lipids with carbon nanotubes (CNTs)³⁷ and with membrane proteins,³⁴ spherical to rodlike transitions in micellar assemblies of surfactants,³⁵ photoinduced self-assembly of azo-containing amphiphiles,³⁶ and self-assembly of three-armed ABC star polyphiles into mesoscale structures.³⁸ If

we have CG models that are available having effective beads representing a small number of atoms, and then well-connected to an atomic/molecular description, they can be used in a multiscale fashion to obtain finer descriptions of the simulated systems through reverse-mapping techniques.^{39–42} This multiscale approach was successfully applied to several soft matter systems,^{43–47} and has been employed, for example, in the context of self-assembly, to relax atomistic models of single-component micelles formed by lysophospholipids of different chain lengths.⁴⁸ Finally, a CG model of TX-100 based on the MARTINI force field introduced by Muddana et al.¹⁷ has been employed to study lipid phase separation in mixed lipid bilayer systems.

Recently, some CG approaches based on particle continuum bridging have been proposed.^{49–61} In particular, molecular models developed in a hybrid particle-field (PF) scheme, combining particles with a field representation, are becoming popular.^{51,56,60–62} This novel approach, because of its computational efficiency, allows one to simulate systems on large time and length scales using CG models close to an atomistic description, i.e., having a large number of particles.^{54,57,58,63–65}

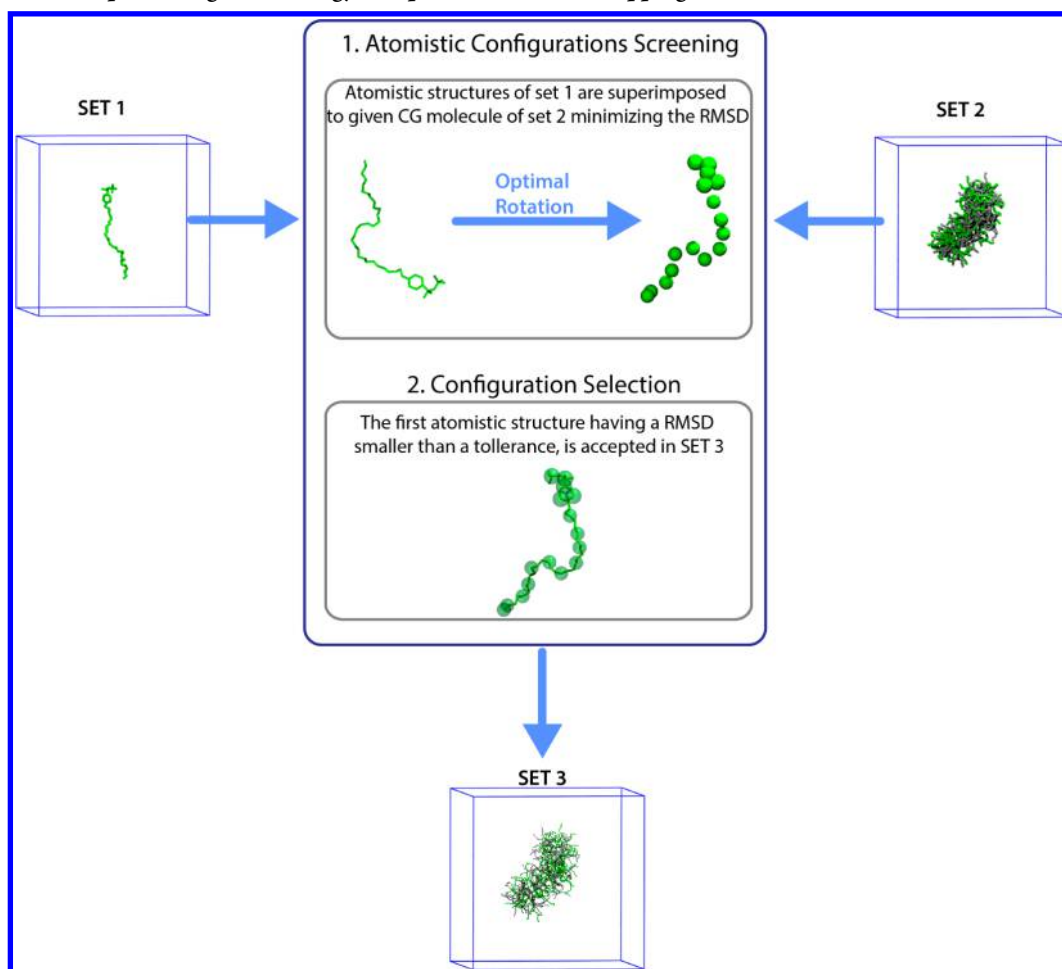
In the framework of a hybrid scheme, MD combined with the self-consistent field (SCF) theory, a technique which we hereafter will reference as “MD-SCF”, has been successfully utilized to study the self-assembly of biocompatible surfactants (Pluronic),⁵⁷ biological phospholipids^{58,63} to model vesicles,^{64,65} and polymer melts⁵⁹ with atomistic or specific CG models. These models allow, at the same time, a resolution close to atomistic (typically three heavy atoms per bead, 3:1 mapping) or an atomistic resolution and access to large scales. As an example, these models are allowed to characterize the interaction and the dynamics of chain release of an entire Pluronic micelle (diameter of ~ 12 nm) containing ibuprofen and model drugs having different hydrophobicities through a lipid bilayer.⁵⁴

With these precedents, in the present study we propose and validate a hybrid CG model of TX-100 in a wide range of concentrations ranging from micellar to hexagonal phases. Detailed atomistic models obtained by a suitable reverse mapping procedure are also proposed and validated against several experimentally available structural and hydrodynamic properties.^{10,66}

The paper is organized as follows. In the [Methods](#) section, a brief description of the MD-SCF computational technique is outlined (more details are given in the [Supporting Information](#) section); moreover, in the same section, hydrodynamic calculations and the reverse mapping procedure are also described. The [Simulation Details](#) section contains information about simulations settings for both CG and atomistic models. This section contains also methodological details and a full list of parameters for both CG and atomistic models. The main results are reported in the [Results and Discussion](#) section. The [Conclusions](#) section summarizes the findings of the study.

METHODS

Hybrid MD-SCF Simulation Technique. The molecular models considered here were developed in a hybrid MD-SCF scheme combining particles and field representations for nonbonded interactions. In the frame of self-consistent field (SCF) theory, the interaction of a particle with other nonbonded particles is considered only through a mean field.

Scheme 1. Scheme Representing the Strategy Adopted for Reverse-Mapping^a

^aSET 1 corresponds to atomistic configurations obtained from the TX-100 single-chain trajectories (15 ns) at 293 K (systems L-I to L-IV in Table 1). SET 2 is a given coarse-grained (CG) configuration to be back-mapped. SET 3 is the back-mapped atomistic configuration.

The Hamiltonian of a system composed of M molecules can be split into two parts:

$$\hat{H}(\Gamma) = \hat{H}_0(\Gamma) + \hat{W}(\Gamma) \quad (1)$$

In eq 1, Γ is a point in phase space and is used to represent a set of positions of all atoms in the configuration of the system; and the “ \wedge ” symbol (hat) means that the related physical quantity is a function of the microscopic states corresponding to the configuration Γ . $\hat{H}_0(\Gamma)$ is the Hamiltonian of a reference system, which, in the present case, is a system composed of molecules interacting only through the intramolecular bonding parameters (bond, angle, etc.) typically considered in MD simulations and $\hat{W}(\Gamma)$ is the deviation from the reference system due to nonbonded interactions.

Below, the partition function of the system assuming a canonical (NVT) ensemble is reported:

$$z = \frac{1}{M!} \int d\Gamma \exp\{-\beta[\hat{H}_0(\Gamma) + \hat{W}(\Gamma)]\} \quad (2)$$

where $\beta = 1/(k_b T)$.

The number density of particles, from a microscopic viewpoint, can be defined as a sum of delta functions placed at the center of mass of each particle:⁶¹

$$\hat{\phi}(\mathbf{r}; \Gamma) = \sum_{p=1}^M \sum_{i=0}^{S(p)} \delta(\mathbf{r} - \mathbf{r}_i^{(p)}) \quad (3)$$

$S(p)$ is the number of particles of the p th molecule and $\mathbf{r}_i^{(p)}$ is the position of the i th particle in the p th molecule. The term $\hat{W}(\Gamma)$ is calculated by assuming that this interaction term is dependent on Γ but only through the particle number density $\hat{\phi}(\mathbf{r}; \Gamma)$:

$$\hat{W}(\Gamma) = W[\hat{\phi}(\mathbf{r}; \Gamma)] \quad (4)$$

The notation $W[\hat{\phi}(\mathbf{r}; \Gamma)]$ means that W is a functional of $\hat{\phi}(\mathbf{r}; \Gamma)$. Starting from these two main assumptions eq 2, using an exact mathematical transformation (namely, the Hubbard–Stratonovich transformation⁶⁷) can be rewritten as a partition function of single molecules in an external field. The nonbonded interaction potential is calculated as an external potential $V(\mathbf{r})$, because of the density fields, on single particles. Details about the proper derivation of $V(\mathbf{r})$ are reported in the Supporting Information. According to this derivation, the mean field solution (using saddle point approximation) for $V(\mathbf{r})$ is

$$V_K(\mathbf{r}) = \frac{\delta W[\{\phi_K(\mathbf{r})\}]}{\delta \phi_K(\mathbf{r})} = k_B T \sum_{K'} \chi_{KK'} \phi_{K'}(\mathbf{r}) + \frac{1}{\kappa} \left(\sum_K \phi_K(\mathbf{r}) - 1 \right) \quad (5)$$

where $\chi_{KK'}$ are the mean field parameters for the interaction of a particle of type K with the density fields due to particles of type K' . The second term on the right-hand side of eq 5 is the relaxed incompressibility condition, where κ is the compressibility, which is assumed to be sufficiently small.

The computational advantage of the hybrid MD-SCF scheme is that the calculation of the nonbonded forces, the most expensive part of the MD simulations, is replaced by the evaluation of forces between single particles with an external potential. For the calculation of these forces, a smooth CG density function, calculated using the particle positions Γ , is needed. The details about this procedure are reported in the [Supporting Information](#).

Reverse Mapping. The quick generation of well-equilibrated atomistic structures is an important task of CG models. In the case of polymeric materials, reverse mapping procedures have been extensively applied. The first polymers to be equilibrated in this way were polycarbonates.^{41,42} More recently, reverse mapping procedures have also been applied to polystyrene^{44,68} and to study gold nanoparticle/polymer interfaces.⁶⁸ The extension of reverse mapping to non-equilibrium situations, such as the determination of the rheology, has been recently demonstrated for atactic polystyrene under steady shear flow.⁶⁹ In the following, the proposed strategy for the reverse mapping of TX-100 is explained in detail.

The strategy chosen for the reverse mapping is based on the rigid superposition (rotation) of chains of TX-100 atomistic models on the CG ones obtained from the mesoscale simulations.⁷⁰ In particular, as reported in [Scheme 1](#), for a given CG molecule, several trial atomistic structures, taken from a structure library, can be superimposed in order to minimize the root-mean-square deviation (RMSD) between the center of the CG beads and the corresponding atomic sites. In order to give enough flexibility to this procedure, the structure library is made of configurations taken from atomistic MD simulations of a single molecule of TX-100 (see [Table 1](#)) in

Table 1. System Composition for Atomistic Models

system	TX-100		water	NaCl	box (nm ³)	time (ns)
	$n = 10$	$n = 9$				
L-I	1	0	802		3.0 ^a	15
L-II	0	1	802		3.0	15
L-III	0	1	802	30	3.0 ^a	15
L-IV	1	0	802	30	3.0 ^a	15
S-I	70	73	61008	60	$11.736 \times 15.097 \times 11.299$	90

^aCubic box.

water as the explicit solvent (SPC/E model) and in the presence of Na⁺ and Cl[−] ions corresponding to a concentration of 0.01 M.⁶⁶ From the systems shown in [Table 1](#), 2000 configurations have been used for both single chains of TX-100 in water (systems L-I, L-II) and a single Triton chain in NaCl solution (systems L-III, L-IV). For a molecule that, after

rotation, is able to maximize the superposition between the center of the CG beads and their corresponding atomic sites (see [Scheme 1](#)), a given trial atomistic structure is accepted if the maximum value obtained for the RMSD between two sites is smaller than a fixed tolerance. For the systems under investigation, a value of tolerance of 0.2 nm has been found to be a good choice.

Pair Distance Distribution Function and Hydrodynamic Computations. To assess the validity of the generated TX-100 atomistic models, we have computed their pair distance distribution function $P(r)$ and their hydrodynamic properties, to be compared with experimental data. The hydrodynamic parameters utilized were the infinite-dilution translational diffusion constant $D_{t(20,w)}^0$, sedimentation coefficient $s_{(20,w)}^0$ (where the subscript “(20,w)” refers to the standard conditions for the viscosity and density of the solvent (water) at 20 °C), and the intrinsic viscosity $[\eta]$. The $P(r)$ were computed to be compared with their experimentally derived counterparts, which were calculated by inverse Fourier transformation from small-angle X-ray scattering (SAXS) data.⁷¹ All the calculated $P(r)$ data have been obtained from reverse-mapped models (i.e., having all non-hydrogen atoms included). The $P(r)$ computation was thus performed using the SAXS settings in the SAS module of the UltraScan Solution MOdeler (US-SOMO; <http://www.somo.uthscsa.edu/>) suite, which utilizes conversion tables where the proper atom definitions and hybridizations are defined; this program also provides a graphical utility for the comparison with the experimentally derived data.^{72,73} For polydisperse systems, the calculated $P(r)$ data are obtained as a weighted sum of partial $P(r)$ data coming from different aggregates. The weights (as reported in [Table S9](#) in the Supporting Information) are obtained by combining frequency values (as calculated from the histogram of [Figure 3](#), presented later in this work) and z -weights.

The hydrodynamic parameters were calculated using standard procedures in rigid body macromolecular hydrodynamics, not employing direct simulation of the trajectory but, e.g., the computation of the resistance matrix for an array of spheres.⁷⁴ In particular, we employed the SoMo bead modeling method⁷⁵ available in US-SOMO,^{72,76} but applying the new approach that was recently proposed,⁷⁷ that is, without bead overlap removal and utilizing the Zeno computational method.^{78–80} Tests with geometrical bodies and selected proteins have shown that $D_{t(20,w)}^0$ and $[\eta]$ can be computed with accuracies within $\pm 4\%$ in both cases.^{78–80}

■ SIMULATION DETAILS

Hybrid MD-SCF simulations of CG models were run with the code OCCAM⁵⁵ in the NVT ensemble, in which the temperature was controlled using an Andersen thermostat⁸¹ (collision frequency = 7 ps^{−1}). All of the simulations (see [Table 2](#)) were conducted at 298 K. A time step of 0.03 ps was employed in all simulations. The density field was updated using a value of $\Delta t_{\text{update}} = 9$ ps. For the density mesh, a grid size of 0.6 nm has been employed for all systems. Both parameters, Δt_{update} and the grid size (l), have been chosen in order to give good reproduction of reference classical MD simulations, as reported in previous studies.^{54,57,58,63}

The MD simulations of atomistic models were carried out with GROMACS 4.5.1^{82,83} in the NVT ensemble at the same temperatures employed for the MD-SCF simulations. The temperature was held constant with a Berendsen thermostat⁸⁴

Table 2. System Composition for CG Models

system	TX-100		CG water	total number of particles	box (nm) $x = y = z$	TX-100 %w/w	concentration [mM]	time (μ s)
	$n = 10$	$n = 9$						
I	140	140	360000	364 340	35	0.8	10.8	6.25
II*	140	140	124040	128 380	25	2.2	29.7	16.0
III	1000	1000	86 805	117 805	23.1	20	269.4	5.8
IV	1500	1500	96 698	143 198	26	35	283.4	12.0
V	1500	1500	53 000	99 500	24	50	360.3	16.0
VI	2000	2000	57 777	119 777	22	60	623.8	5.8
VII	2000	2000	49 600	111 600	21.5	70	668.3	5.8
VIII	2500	2500	54 253	131 753	22.5	80	728.9	5.8

* For system II, five independent simulations have been performed, each one for a time of 16 μ s.

($\tau_T = 0.1$ ps). A time step of 0.002 ps was employed for all atomistic simulations. For both van der Waals and Coulomb interactions, a cutoff distance of 1.2 nm was employed. The long-range corrections to electrostatic interactions were calculated using a Particle Mesh Ewald method.⁸⁵ The Lincs constraint algorithm⁸⁶ has been applied to all bonds in the atomistic simulations. A full list of parameters for both CG and atomistic models is reported in the [Supporting Information](#).

RESULTS AND DISCUSSION

A first validation of the proposed CG model has been done for low TX-100 concentrations. In particular, the CMC of the Triton model has been investigated. [Figure 1](#) shows the fraction

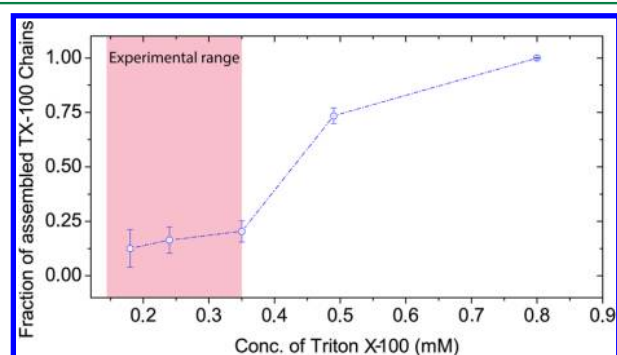


Figure 1. Fraction of assembled Triton X-100 chains at different concentrations, corresponding to the systems listed in [Table S8](#) of the [Supporting Information](#). Chains are considered assembled if the number of neighbors is greater than zero. The neighbors are calculated on the base of cutoff criterion (1 nm) on the shorter distance between two beads of two different chains. Each point in the plot corresponds to the average on the last microsecond of each simulation.

of assembled TX-100 chains, as a function of concentration, compared with the experimental value of the CMC. From the behavior of the assembled chains fraction, we can observe that, for concentrations of <0.49, a sharp decrease of the assembled chains is found, in agreement with the experimental range (0.14–0.35 mM).^{87,88}

[Figure 2](#) shows the time behavior of some simulated systems during the assembly process, obtained starting from a random mixture of TX-100 surfactant molecules in water at different concentrations. Three different concentrations corresponding to micellar phases (systems I, II, and IV, having a TX-100 concentration below the boundary of the hexagonal phase, as reported from experimental studies^{25,26}) have been considered.

From the snapshots of [Figure 2](#), it is clear that micellar assemblies are made of aggregates of different sizes

(polydispersity) and shapes. Higher concentrations of TX-100 correspond to higher aggregation numbers (N_{agg}). This behavior is in agreement with quenching fluorescence measurements,⁸⁹ and these data can be directly compared with average aggregation numbers obtained from simulations. In particular, for system I (0.8% w/w), the calculated aggregation number ($N_{\text{agg}} = 20$ –60) can be compared with the average aggregation number measured at 1% w/w ($N_{\text{agg}} = 80$) at the same temperature of the simulations. For system II at higher TX-100 concentration (2.2% w/w), the calculated N_{agg} values (100–160) are within the range that has been reported by several authors (100–140).^{10,90–92} In order to compare higher moments of size distribution of the micelle, SAXS data are available at the same TX-100 concentration. In particular, Wilfing et al.⁹³ reported average N_{agg} values of 141 (at 293 K) and 290 (at 303 K), and these data can be compared by z-averaging (weights are proportional to N^3 ; the mathematical definition of z-average is reported in the [Supporting Information](#)) of the aggregation numbers obtained from simulations. In particular, for system II, at a TX-100 concentration of 2.2% w/w, an averaged aggregation number of $\langle N_{\text{agg}} \rangle_z = 130$ –230 is calculated. As an example, in [Figure 3](#), the number of TX-100 molecules/micelles calculated according to a clustering algorithm are reported for system II (2.2% w/w), where five independent simulations have been considered. From both [Figures 3A](#) (average number of TX-100 per micelle) and [3B](#) (number of TX-100 in biggest aggregate), it is clear that, for all simulations, the systems complete the self-assembly process and reach an equilibrium distribution having aggregates of fluctuating size after ~ 5 μ s.

The overall picture emerging from the simulation results is a polydisperse mixture of micelles of different size and shapes, and this behavior is in agreement with several measurements of static and dynamic properties reported in the literature for aqueous solutions of TX-100.^{88,89,97} In particular, comparisons between diffusion coefficients measured by pulsed-field-gradient NMR and quasi-static elastic scattering techniques give indications of the polydisperse nature of TX-100 micelles.⁸⁹ In [Figure 3C](#), the aggregate size (N of the TX-100 molecule/cluster) calculated from MD simulations, obtained averaging over the last 10 μ s of the five independent simulations, for system II (2.2% w/w TX-100), together with the experimental^{10,91,93} average aggregation number, obtained from different techniques, are reported.

The fair agreement between simulations and experimental aggregation behavior coming from different techniques indicates that the model systems are able to reproduce the distribution of micelle sizes correctly. For a more-detailed characterization of the micelle structural features, it is possible

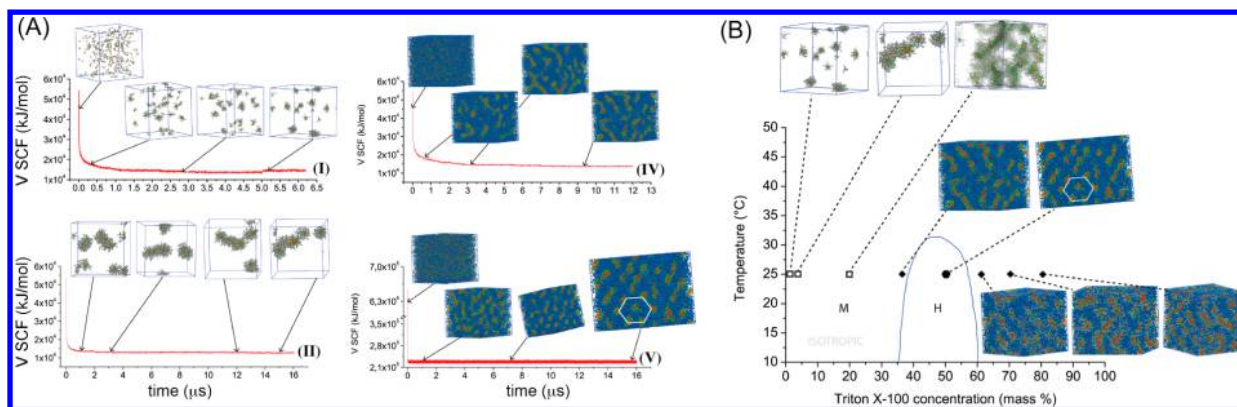


Figure 2. (A) Time evolution of SCF potential for TX-100/water mixture at different compositions. The composition of the systems reported in the figure is reported in Table 2. (B) Phase diagram for Triton X-100. For any composition and temperature investigated, a snapshot of the morphology, at equilibrium, is superimposed on the diagram. The phase diagrams is redrawn from ref 26.

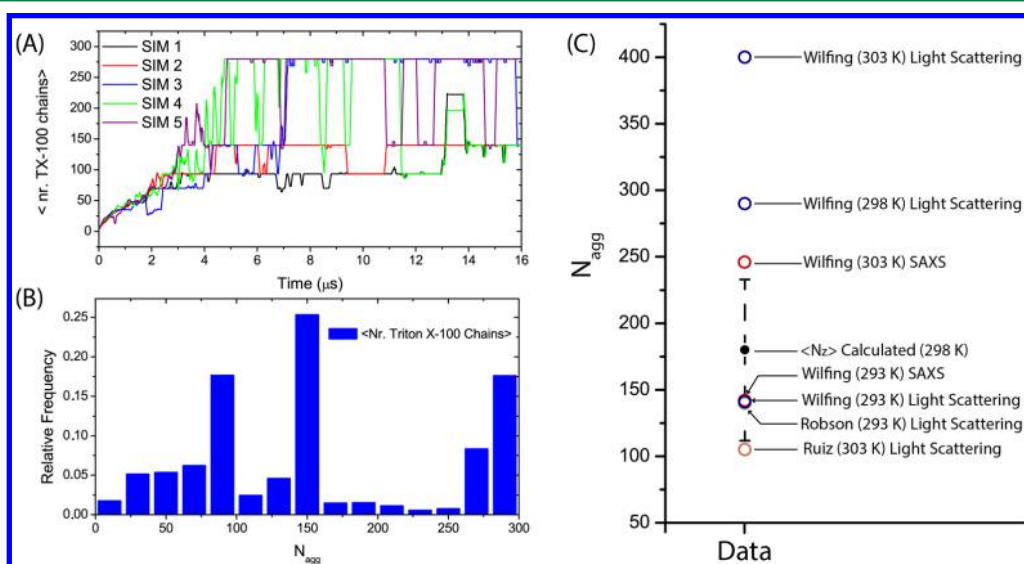


Figure 3. (A) Time evolution of the average cluster size of Triton micelles. (B) Size distribution of Triton X-100 aggregates. (C) Comparison of calculated N_{agg} (filled black point) and N_{agg} experimentally obtained from different techniques (open circles). The algorithm GROMOS used to identify the aggregates of Triton X-100 is a nonhierarchical cluster algorithm based on a self-organizing neural net.^{94–96} The criterion for clustering is that all conformations in a cluster must be within a specified cutoff distance. The cutoff that we used to determine the cluster size distribution is $r_{cut} = 1.0$ nm.

to compare calculated and experimentally available pair distance distribution functions $P(r)$. The $P(r)$ value is calculated considering the distribution of calculated distances between a pair of atoms (i.e., the frequency of a given distance between any pair of atoms). In particular, the $P(r)$ value has been calculated using atomistic structures obtained from reverse mapping procedures of micellar assemblies derived from the CG simulations of system II. Atomistic structures have been obtained using the procedure outlined in Scheme 1. Technical details about the reconstruction of atomistic degrees of freedom starting from CG coordinates are reported in the reverse mapping section. As an example, in Figure 4, the CG and the reverse mapped atomistic models are depicted for a micelle made of 280 TX-100 molecules. For the CG models, two different colors in the figure (gray and green) correspond, according to experimental chain length distribution,¹⁰ to PEO chains having 9 and 10 EO units, respectively. Self assembled structures have been obtained from all considered systems, starting from a mixture having 50% of TX-100 chains having 9 and 50% of TX-100 chains having 10 EO units.

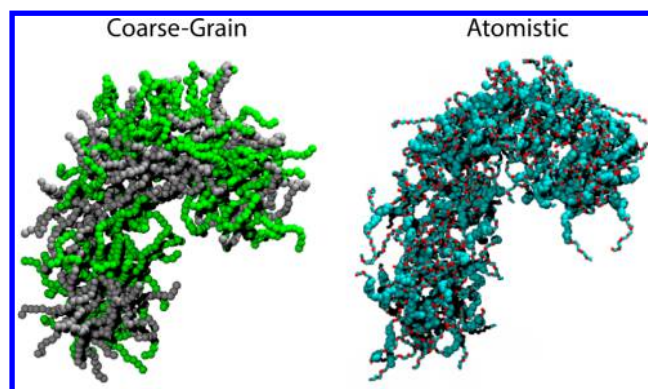


Figure 4. CG TX-100 micelle with $N_{agg} = 280$ chains on the left side. The green chains correspond to TX-100 with 10 EO units. The gray chains correspond to the TX-100 chains with 9 EO units. On the right side are reported the atomistic micelle obtained applying the reverse mapping procedure.

In Figure 5A, the weighted $P(r)$ calculated from atomistic micelle models obtained by back mapping of CG configurations

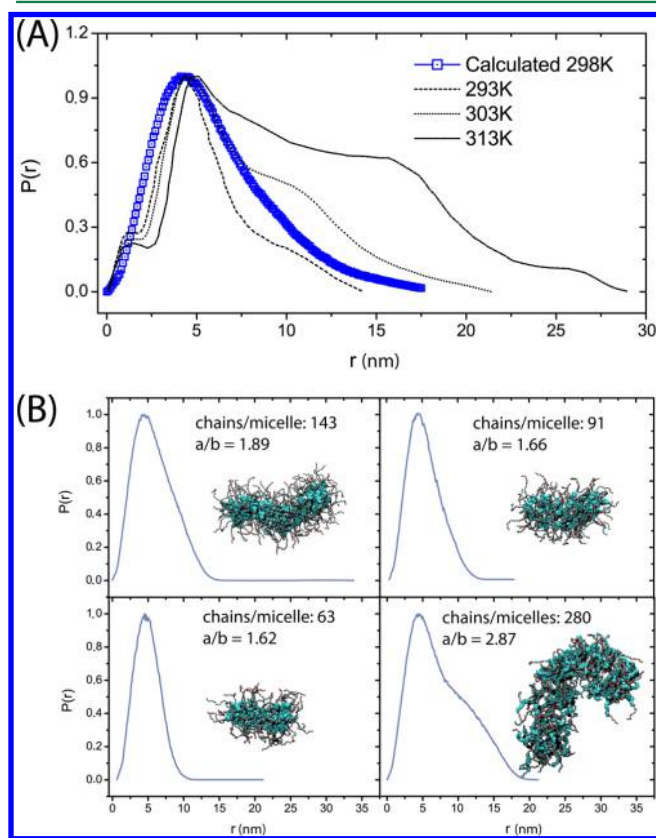


Figure 5. (A) Experimental⁹³ and calculated pair distance distribution functions $P(r)$. The calculated $P(r)$ values reported in the figure are weighted sums of partial $P(r)$ values obtained from different aggregates. The weights (reported in Table S9) are obtained by combining frequency (lifetime) and z-weights. (B) Calculated $P(r)$ values for the main micellar aggregates.

of system II, together with available experimental data at the same TX-100 concentrations at three different temperatures, are reported. The behavior of pair distribution functions at different temperatures is interpreted in terms of different aggregation numbers. In particular, because of a weakening of hydrogen bonds between the hydrophilic poly(ethylene oxide) (PEO) chains and water, there is an increase of aggregation number with temperature. In Figure 5B, the individual $P(r)$ values of the main atomistic structures are reported. The position of the maximum of the $P(r)$ is weakly affected by the size of the micelle, and, in all cases, it is ~ 4 nm, corresponding to the thickness of the aggregates. The small shoulder appearing at very short distances is not present in any of the $P(r)$ values calculated for our simulated micelles, and it is difficult to reconcile it with a specific potential micellar feature. Rather, it could be an experimental artifact resulting from the presence of relatively large amounts of nonaggregated material. Bigger differences can be found in the behavior at longer distances (between 10 and 20 nm). This region of the $P(r)$ values is strongly dependent on the aggregation number. Indeed, for the smaller micelle ($N_{\text{agg}} = 63$), the $P(r)$ value reported in Figure 5B in this region is zero. For larger aggregates, the $P(r)$ values are characterized by a shoulder that is more pronounced for higher aggregation numbers (see, e.g., the $P(r)$ value of the micelle having $N_{\text{agg}} = 280$). The behavior

of individual $P(r)$ values, corresponding to different N_{agg} values, is consistent with the different shapes of the experimental ones at low and high temperatures and the behavior of N_{agg} with temperature. In particular, because of a weakening of hydrogen bonds of EO units with water molecules at higher temperatures, TX-100 accordingly shows an increase of aggregation number. Indeed, the change in the experimental $P(r)$ values with temperature involves mainly the region at $r > 10$ nm, with an increase of the shoulder, that in our calculated $P(r)$ corresponds to the contribution of structures with high aggregation number. It is important to point out that the calculated pair distribution function corresponds to simulations performed at 298 K. This temperature has been selected for our study on the basis of biological applications of the models. Indeed relevant measurements also in the presence of electrolytes have been performed by Paradies⁶⁶ at 298 K. Models suitable for these systems are discussed later, but it would have been too costly, in terms of computing times, to repeat the simulation at each experimental temperature for the systems in water that have been discussed above.

In Figure 6, the behavior of the asphericity (a/b), as a function of N_{agg} is reported together with some snapshots. The

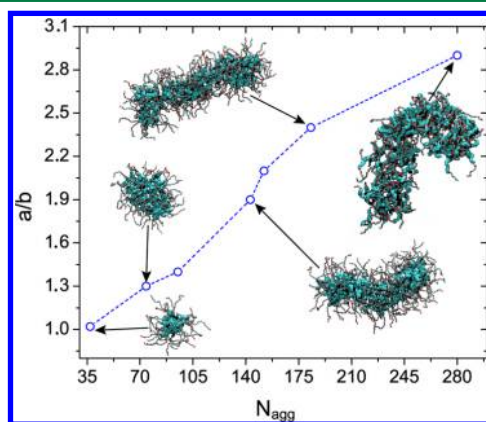


Figure 6. Ratio a/b between the two semi axes a and b of an ellipsoid is reported for micelle having different N_{agg} . The semi axes are calculated from the radius of gyration evaluated along the direction of the main inertia axes of each micelle.

sizes a and b are the semi axes of an ellipsoid calculated from the components of the radius of gyration along the direction of the main inertia axes of the micelle. Figure 6 clearly shows that, when going from low N_{agg} values to high N_{agg} values, a transition from spherical ($N_{\text{agg}} \approx 37$) to nonspherical shapes is apparent. The calculated behavior is in agreement with the interpretation of diffusion data of Denkova et al.⁸⁸ In particular, a nonlinear increase in hydrodynamic micellar radius with TX-100 concentration, obtained from NOESY NMR measurements, has been interpreted as a possible sphere-to-rod transition.

Generally, from an experimental point of view, direct information about the micelle shape is not easy to be obtained. Indeed, the same experimental pair distance distribution function can be compatible with different hypothetical shapes. For this reason, the issue about the TX-100 micelle shape is still an open one. Additional indication about the micelle shape can be obtained from the hydrodynamic behavior, especially from $[\eta]$ which is very sensitive to the shape of the aggregates. On this basis, Robson and Dennis,¹⁰ considering two possible

shapes (prolate and oblate), concluded that, based on their data, the preferred shape for $N_{\text{agg}} = 140$ is an oblate shape with an a/b ratio of 1.9. The same value can be calculated for micelles with the similar N_{agg} as reported in Figure 6. Wilfing⁹³ gave some indications about possible oblate and spherical shapes. More recently, Denkova et al.,⁸⁸ using NOESY NMR diffusion measurements, found for diluted aqueous TX-100 solutions, data consistent with spherical shapes, at concentrations between 2% and 6% w/w. Our simulations show polydisperse micellar aggregates. In particular, for the most diluted (TX-100 0.8% w/w) system I (see Figure 2), a preference for spherical micelles is found. For system II, occurrence of spherical, oblate, and prolate shapes have been found. The shape of the micellar aggregates is dependent mainly on the aggregation number. In Figure 7, typical shapes

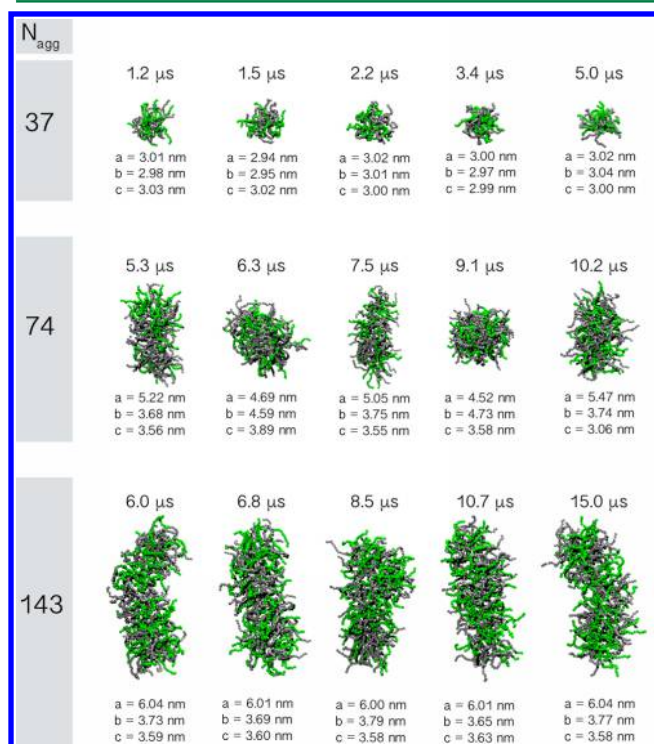


Figure 7. Snapshots of TX-100 micelles, at different N_{agg} corresponding to different configurations along simulation time (reported on the top of each snapshot). Below each snapshot, the lengths of the main axes of the micelle are reported. An ellipsoid is oblate if there are two long axes (approximately of the same length) and a short one. A prolate ellipsoid has one long axis and two short axes (approximately of the same length).

found in the simulations of systems I and II are reported. In particular, for low aggregation numbers, a spherical shape is observed. This shape, as reported in Figure 7, is stable along the entire lifetime of the micelle. A similar behavior is found for micelles having $N_{\text{agg}} \approx 140$ or larger showing a stable prolate shape. Differently, as shown in Figure 7, for an intermediate $N_{\text{agg}} \approx 70$ fluxional form, alternating (on a time scale of 1 μs) prolate and oblate shapes are found.

These results are consistent with a microscopic analysis of shape transition performed by other authors.^{98–101} These authors, using bidimensional mean field theory calculations, reported that the free-energy profile was a function of N_{agg} for an asymmetric linear surfactant. They show a complex free-energy behavior with multiple minima corresponding to

spherical, oblate, and cylindrical shapes, depending on N_{agg} . This shape transition from spherical to nonspherical upon increasing the surfactant concentration, is characterized by a coexistence region where spherical, oblate, and prolate shapes are thermodynamically stable for values of $N_{\text{agg}} \approx 70$, while for $N_{\text{agg}} = 12–140$, the prolate shape is found to be predominant.⁹⁸

Several studies on TX-100 micelles have been focused on systems in the presence of electrolytes, for their relevance in mimicking physiological environments.^{66,92} The main effect due to the presence of ions is a more compact form of the micelles. In Figure 8, we report the $P(r)$ calculated by Paradies et al.⁶⁶

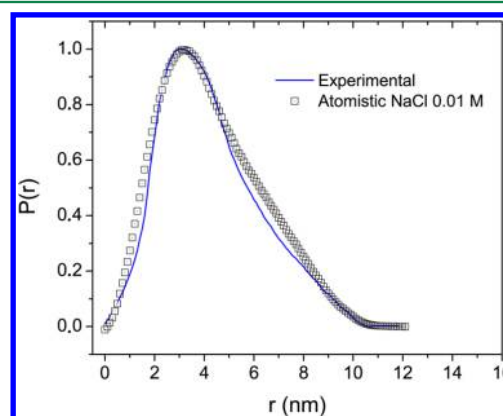


Figure 8. Experimental (blue curve) and calculated (symbols) $P(r)$ for a TX-100 micelle in a water solution containing NaCl 0.01 M.

from SAXS data collected on a monodisperse ($N_{\text{agg}} \approx 140$) solution of TX-100 micelles, obtained by introducing a size-exclusion chromatography step before the measurements, in the presence of 0.01 M $[\text{NaH}_2\text{PO}_4]$ (solid blue line). As can be seen by comparing Figures 5 and 8, the presence of ions shifts the maximum of the $P(r)$ values to shorter distances, from 4.3 nm in pure water to 3.1 nm in 0.01 M $[\text{Na}^+]$. An atomistic model of the micelle in the presence of NaCl has been obtained by implementing a suitable reverse mapping procedure. In particular, the reverse mapping scheme is applied using as atomistic structure library (Set 1 in Scheme 1) of a single-chain simulation of TX-100 in the presence of explicit Na^+ and Cl^- ions at the concentration of 0.01 M. As shown in Figure 8, the calculated $P(r)$ obtained from the atomistic model is in very good agreement with the curve derived from the SAXS experiments. The more-compact shape of TX-100 micelles has been ascribed to a partial dehydration of the hydrophilic PEO shell of the micelle in the presence of ions. In particular, the dehydration of the polar shell of the micelle can be ascribed exclusively to the nature of the cation, as reported in different studies.^{66,92,97} This hypothesis is supported by the behavior of the diffusion coefficient obtained by light scattering experiments and electronic paramagnetic resonance studies.^{92,97} In Figure 9, the effect of ions on TX-100 chain size is analyzed. In particular, distributions of R_g for the TX-100 chain in the presence of NaCl is compared with that in pure water in Figure 9A. From this figure, it is clear that, in the presence of ions, the TX-100 chain is more compact. The distributions of hydrogen bonds (Figure 9B) gives a molecular interpretation of this behavior, showing a decrease of hydrogen bonds between the poly(ethylene oxide) chain of TX-100 and water in the presence of ions.

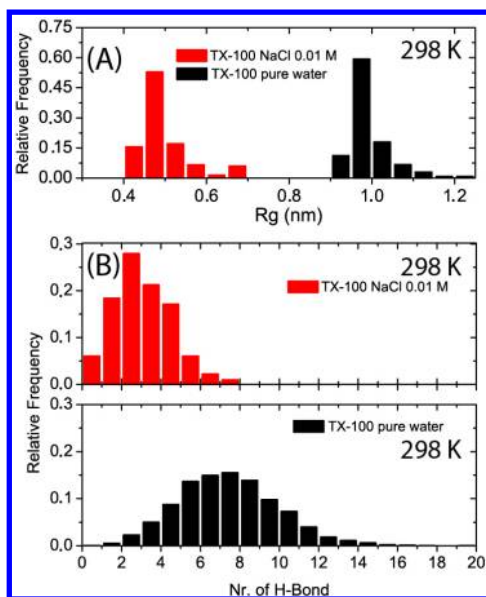


Figure 9. (A) R_g distributions calculated for a single TX-100 chain in pure water and in a NaCl/water solution. (B) Hydrogen bond distributions calculated between the hydrogen donor of water molecules and the oxygen atoms of the EO groups (acceptor) of the TX-100 chain, for a chain in pure water and in a NaCl solution. The hydrogen bonds are calculated considering, as geometrical criteria, a cutoff distance of 0.30 nm and an O–H–O angle of $\theta = 120^\circ$.

The main features of the atomistic model obtained for the TX-100 micelle, in the presence of NaCl, are reported in Figure 10. In particular, the two components of R_g along the main inertia axis and the a/b ratio derived from it for an oblate shape are reported, together with values proposed from experimentally derived models.⁶⁶ As can be seen from the behavior of structural and hydrodynamic properties reported in Figure 10 and in Table 3, the micelle obtained from the reverse mapping procedure is a good starting point for the atomistic simulation. All the properties (for example, the semi axial lengths, as well as their a/b ratio) are stable and only small fluctuations are observed along 90 ns of the simulation. Moreover, although the equilibrium value of the a/b ratio (1.88) is similar to that hypothesized by Paradies (1.78),⁶⁶ we found a different shape (prolate) and a long semiaxis ($a = 6.07$ nm) smaller than that hypothesized by Paradies ($a = 6.89$ nm). In particular, on the basis of the assumed size, Paradies evaluated a volume of $7.6 \times 10^5 \text{ \AA}^3$ for a prolate model, which is not compatible with the experimental volume obtained from SAXS measurement ($4.31 \times 10^5 \text{ \AA}^3$). Our prolate simulated structures, which were different from that proposed by Paradies, having $b \approx c \approx 3.5$ nm and $a \approx 6.07$ nm (Figure 10A), with a volume of $4.32 \times 10^5 \text{ \AA}^3$, are fully compatible with the SAXS experiments. Furthermore, additional comparisons can be done by calculating the hydrodynamic properties. Indeed, comparison with experimental data (diffusion and sedimentation coefficients, intrinsic viscosity) have been made starting from equilibrated micelle configurations and calculating these parameters using SoMo overlapping bead models, followed by Zeno computations (see the Methods section). The results put into evidence that, for the hydrodynamic properties, we also have only small fluctuations in the 90 ns of simulation (Table 3). In particular, the calculated average $S^0_{(20,w)}$, 1.76 ± 0.01 S, and $D^0_{t(20,w)}$, $(5.28 \pm 0.01) \times 10^{-7} \text{ cm}^2/\text{s}$, compare well with the corresponding experimental data obtained by

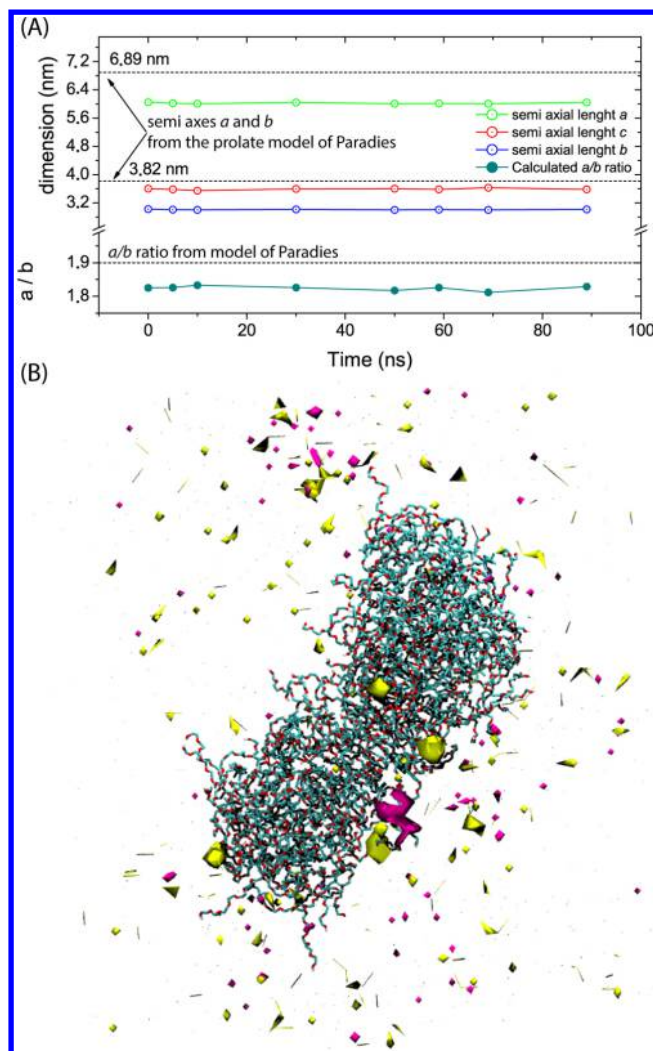


Figure 10. (A) Radius of gyration, asphericity (a/b), and semi axial length of TX-100 micelle, are reported jointly with the experimental values (dashed lines). (B) Snapshot of the micelle structure with the density isosurfaces, where ρ is larger than 0.01 ions/nm³, representing the distributions of Na⁺ and Cl⁻ ions. The composition of the system is reported in Table 1.

Table 3. Hydrodynamic Properties Calculated from the Atomistic Micelle in an Electrolyte/Water Solution

time (ns)	diffusion coefficient $10^{-7} \text{ (cm}^2/\text{s)}$	intrinsic viscosity $\text{(cm}^3/\text{g)}$	sedimentation (S)	partial specific volume $\text{(cm}^3/\text{g)}$	R_H (nm)
0	5.26	4.90	1.76	0.910	3.24
5	5.27	4.90	1.76	0.910	3.24
10	5.28	4.91	1.76	0.910	3.24
30	5.29	4.94	1.76	0.910	3.25
50	5.29	4.84	1.77	0.910	3.24
59	5.28	4.88	1.77	0.910	3.26
69	5.28	4.90	1.76	0.910	3.25
90	5.29	4.88	1.77	0.910	3.25
Paradies ⁶⁶	4.92	5.40	1.67	0.912	2.96

averaging the data for similar N_{agg} reported by Paradies,^{66,104} 1.66 ± 0.05 S and $(4.93 \pm 0.02) \times 10^{-7} \text{ cm}^2/\text{s}$. As for $[\eta]$, our calculated value of $4.88 \pm 0.04 \text{ cm}^3/\text{g}$ compares somewhat less well but still reasonably with an average of the experimental

values of $5.40 \text{ cm}^3/\text{g}$ reported by Paradies.⁶⁶ Considering the approximation made to represent the counterion atmosphere in our simulations, it appears that the hydrodynamics also support our TX-100 micelle model. A snapshot of the atomistic structure of the micelle of TX-100 in NaCl water solution is depicted in Figure 10B; the yellow and magenta regions are density isosurfaces of Na^+ and Cl^- ions, respectively.

As described in Figure 2, for TX-100 concentrations larger than 30% w/w, a region (between 35% and 60% w/w) of the phase diagram appears in which a hexagonal columnar phase is stable. The phase behavior of TX-100 in this region has been characterized by rheological, optical, and X-ray synchrotron techniques^{26,102} and simulations results can be compared with the picture coming from these studies. In Figure 11, density isosurfaces corresponding to hydrophobic beads (types A and B in Scheme S1 of Supporting Information) are reported for systems at different TX-100 concentrations. In particular, for the systems at 35% w/w, the simulations show an assembly of discrete micelles in a disordered orientations (Figure 11A). For

larger concentrations (50%, 60%, and 80% w/w), continuous phases are obtained, starting from randomly mixed systems, in all cases. For the system corresponding to the experimental conditions of ordered phase (50% w/w), the presence of columnar micelles is apparent from the density isosurfaces of Figure 11B. In the same figure panel, for the sake of clarity, some columnar assemblies belonging to the same plane are highlighted, showing the remaining surfaces in gray in two different views. This panel clearly presents columns that show undulations, column bridging, and dislocations. In the schematic picture of Figure 11C, the defective columnar phase is sketched, in particular, the presence of undulations (zigzag shapes) and defects. These structural features are in agreement with the picture and the interpretation given by the phase transition rheology of Triton X-100 water mixture that was reported by Ahir et al.²⁶ In fact, rheological measurements suggest a defect locking mechanism during the formation of the hexagonal phase. The presence of defects causes high rigidity. Further rigidity is provided by column undulations that are able to become entangled with each other, thereby increasing the storage modulus.^{103–105}

A further application of the reverse mapping scheme has been done on the equilibrium structures of columnar phase. In Figure 12A, both atomistic and coarse-grained configurations are reported. Atomistic configurations have been then used to calculate X-ray spectra. In particular, atomistic structures obtained by reverse mapping of the CG system along the self-assembly process have been obtained. Figure 12B shows the time evolution of the intensity of the peak corresponding to a spacing of 6.2 nm (lattice parameter $a = d[2/(3)^{1/2}] = 5.4 \text{ nm}$), in good agreement with the value reported by Ahir et al.²⁶ ($a = 5.9 \text{ nm}$).

CONCLUSIONS

A coarse-grained (CG) model is proposed and validated for TX-100. Although the adopted CG description is close to atomistic models (3:1 mapping), the hybrid particle field formulation of the models allows simulations of large-scale systems (having beads number ranging from 100.000 to 600.000 for simulation times from 5 μs to 15 μs). The CG model has been accurately validated in a wide range of concentrations in aqueous solution; in particular, the critical micelle concentration, shape transition in isotropic micellar phase, and appearance of hexagonal order are well-reproduced in the ranges reported in the experimental literature. The fine resolution of the proposed CG model allows one to obtain, by a suitable reverse mapping procedure, atomistic models of micellar assemblies and for the hexagonal phase. In particular, atomistic models of the micelles give structures in good agreement with experimental $P(r)$ and the shapes hypothesized on the basis of hydrodynamic measurements. For a better comparison with experiments, atomistic coordinates of micelles have been used to calculate, using hydrodynamic modeling, the intrinsic viscosity and the diffusion and sedimentation coefficients in good agreement with available experimental data. The picture emerging by detailed analysis of self-assembly in simulated systems is quite complex. Polydisperse mixtures of spherical-, oblate-, and prolate-shaped aggregates have been found. The shape and the micelle behavior are mainly dictated by N_{agg} of the aggregate. In particular, micelles with low aggregation numbers ($N_{\text{agg}} \approx 40$) are spherical, whereas, for those with high aggregation numbers ($N_{\text{agg}} \approx 140$ or higher), the micelles are characterized by prolate ellipsoidal shapes. For

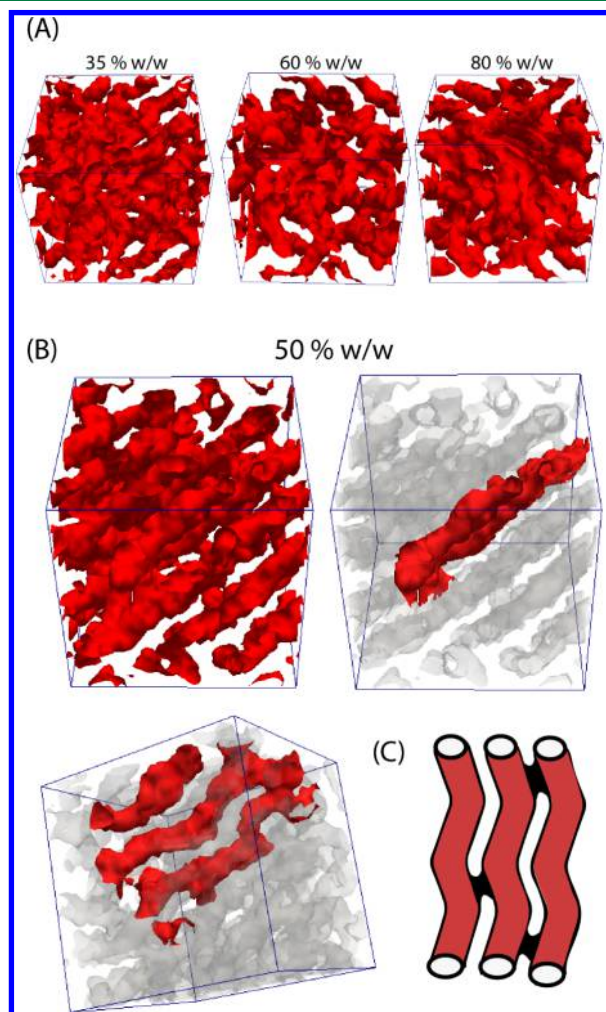


Figure 11. Isosurfaces of hydrophobic beads of Triton chains are reported: (A) systems IV (35% w/w), VI (60% w/w), and VIII (80% w/w); (B) system V (50% w/w). Additional representation of system V, in which part of the columns are highlighted in red, are reported to show in better detail the zigzag morphology of the columns and the defects. (C) Schematic representation of the zigzag morphology; the junction defects are reported. All isosurfaces correspond to a density of $\rho > 0.25 \text{ particles}/\text{nm}^3$.

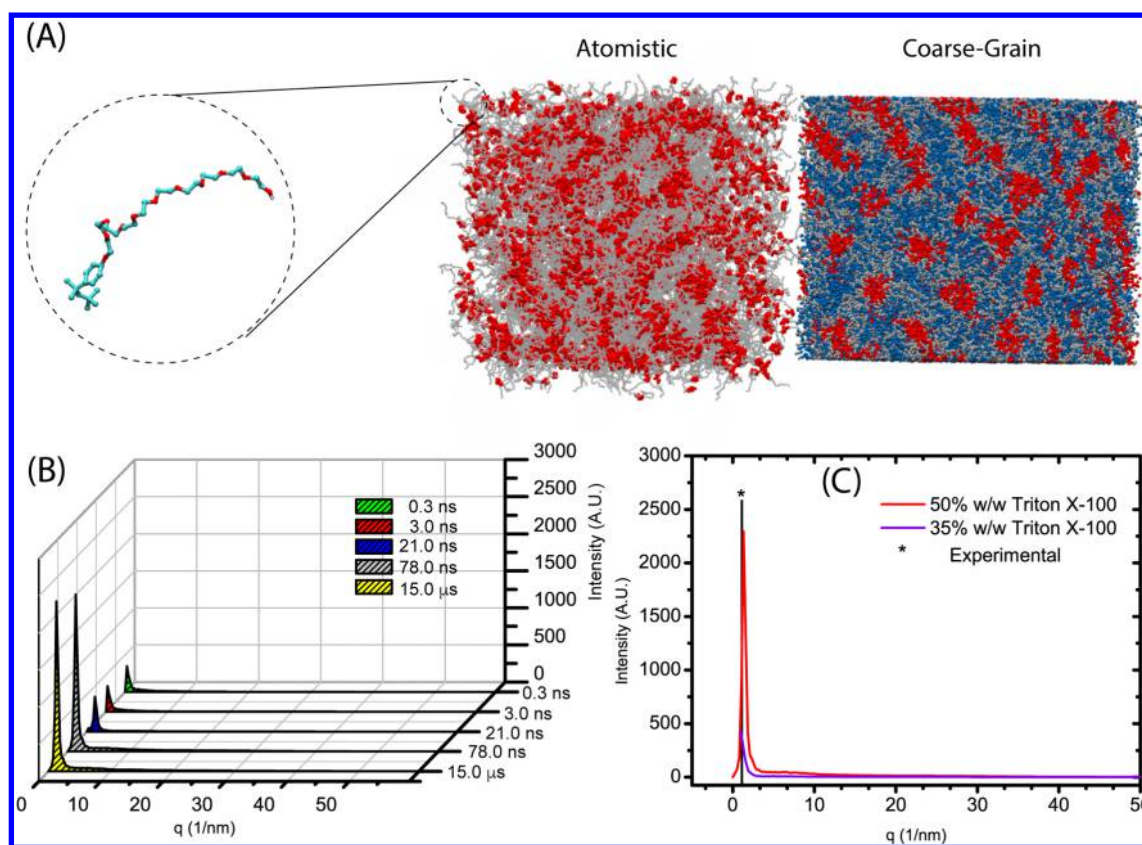


Figure 12. (A) Snapshots of the CG configuration and the atomistic configuration, obtained from the reverse mapping procedure, of system V are reported. Details of the atomistic chain conformation are reported in the expanded view (left). (B) Time evolution of the X-ray spectra for system V. (C) X-ray spectra calculated for systems IV and V, compared with the experimental peak (corresponding to the lattice parameter $a = 5.4$ nm reported by Ahir et al.²⁶).

those with intermediate aggregation numbers ($N_{\text{agg}} \approx 70$), fluxional micelles, alternating between oblate and prolate shapes, are observed.

The proposed model, because of its computational efficiency for parallel applications, opens the way to investigations of several mechanisms involving TX-100 assembly in protein and membrane biophysics. The atomistic structures obtained by the proposed procedure are a solid starting point for further modeling studies of TX-100 at both CG and atomistic levels of detail. Moreover, from a more general point of view, the present study provides a modeling scheme that enables one to obtain accurate models for aggregates made of other surfactants and/or self-assembled molecules.

■ ASSOCIATED CONTENT

Supporting Information

The Supporting Information is available free of charge on the ACS Publications website at DOI: 10.1021/acs.jctc.5b00485.

Parameters for coarse-grained and atomistic models, derivation of SCF potential, definitions of aggregation numbers, description of the method used for hydrodynamic calculations, additional tables including composition of systems for CMC calculation and hydrodynamic properties calculated for the system II (PDF)

■ AUTHOR INFORMATION

Corresponding Author

*E-mail: gmilano@unisa.it. Web page: www.smms.unisa.it.

Funding

G.M. thanks MIUR (FIRB “RETE ITALNANONET”) for financial support.

Notes

The authors declare no competing financial interest.

■ ACKNOWLEDGMENTS

G.M. thanks the HPC team of Enea (<http://www.enea.it>) for using the ENEA-GRID and the HPC facilities CRESCO (<http://www.cresco.enea.it>) in Portici.

■ REFERENCES

- (1) Brown, D. A.; London, E. *Annu. Rev. Cell Dev. Biol.* **1998**, *14*, 111.
- (2) Casadei, B. R.; Domingues, C. C.; de Paula, E.; Riske, K. A. *Biophys. J.* **2014**, *106*, 2417.
- (3) Lasch, J.; Hoffman, J.; Omelyanenko, W. G.; Klivanov, A. A.; Torchilin, V. P.; Binder, H.; Gawrisch, K. *Biochim. Biophys. Acta, Biomembr.* **1990**, *1022*, 171.
- (4) le Maire, M.; Champeil, P.; Møller, J. V. *Biochim. Biophys. Acta, Biomembr.* **2000**, *1508*, 86.
- (5) Lichtenberg, D.; Ahlyauch, H.; Goñi, F. M. *Biophys. J.* **2013**, *105*, 289.
- (6) Koley, D.; Bard, A. J. *Proc. Natl. Acad. Sci. U. S. A.* **2010**, *107*, 16783.
- (7) Gennuso, F.; Ferneti, C.; Tirolò, C.; Testa, N.; L'Episcopo, F.; Caniglia, S.; Morale, M. C.; Ostrow, J. D.; Pascolo, L.; Tiribelli, C.; Marchetti, B. *Proc. Natl. Acad. Sci. U. S. A.* **2004**, *101*, 2470.
- (8) Rajagopal, A.; Pant, A. C.; Simon, S. M.; Chen, Y. *Cancer Res.* **2002**, *62*, 391.

- (9) Hipfner, D. R.; Gaudie, S. D.; Deeley, R. G.; Cole, S. P. C. *Cancer Res.* **1994**, *54*, 5788.
- (10) Robson, R. J.; Dennis, E. A. *J. Phys. Chem.* **1977**, *81*, 1075.
- (11) <http://www.ncbi.nlm.nih.gov/pubmed>, 2015.
- (12) <http://www.rcsb.org/pdb/home/home.do>, 2015.
- (13) Akey, D. L.; Brown, W. C.; Dutta, S.; Konwerski, J.; Jose, J.; Jurkiw, T. J.; DelProposto, J.; Ogata, C. M.; Skiniotis, G.; Kuhn, R. J.; Smith, J. L. *Science* **2014**, *343*, 881.
- (14) Schauder, C. M.; Wu, X.; Saheki, Y.; Narayanaswamy, P.; Torta, F.; Wenk, M. R.; De Camilli, P.; Reinisch, K. M. *Nature* **2014**, *510*, 552.
- (15) Jones, M. N. *Int. J. Pharm.* **1999**, *177*, 137.
- (16) Ingelmo-Torres, M.; Gaus, K.; Herms, A.; González-Moreno, E.; Kassar, A.; Bosch, M.; Grewal, T.; Tebar, F.; Enrich, C.; Pol, A. *Biochem. J.* **2009**, *420*, 373.
- (17) Muddana, H. S.; Chiang, H. H.; Butler, P. J. *Biophys. J.* **2012**, *102*, 489.
- (18) Preté, P. S. C.; Domingues, C. C.; Meirelles, N. C.; Malheiros, S. V. P.; Goñi, F. M.; de Paula, E.; Schreier, S. *Biochim. Biophys. Acta, Biomembr.* **2011**, *1808*, 164.
- (19) Heerklotz, H.; Seelig, J. *Biophys. J.* **2000**, *78*, 2435.
- (20) Sáez-Cirión, A.; Alonso, A.; Goñi, F. M.; McMullen, T. P. W.; McElhaney, R. N.; Rivas, E. A. *Langmuir* **2000**, *16*, 1960.
- (21) Sudbrack, T. P.; Archilha, N. L.; Itri, R.; Riske, K. A. *J. Phys. Chem. B* **2011**, *115*, 269.
- (22) Mani, G.; Pushparaj, H.; Peng, M. M.; Muthiahpillai, P.; Udhumansha, U.; Jang, H. T. *Mater. Res. Bull.* **2014**, *51*, 228.
- (23) Serra, A.; Gomez, E.; Caldero, G.; Esquena, J.; Solans, C.; Valles, E. *Phys. Chem. Chem. Phys.* **2013**, *15*, 14653.
- (24) Wang, Y.; Wang, X.; Antonietti, M.; Zhang, Y. *ChemSusChem* **2010**, *3*, 435.
- (25) Beyer, K. J. *Colloid Interface Sci.* **1982**, *86*, 73.
- (26) Ahir, S. V.; Petrov, P. G.; Terentjev, E. M. *Langmuir* **2002**, *18*, 9140.
- (27) Derecskei-Kovacs, A.; Derecskei, B.; Schelly, Z. A. *J. Mol. Graphics Modell.* **1998**, *16*, 206.
- (28) Yordanova, D.; Smirnova, I.; Jakobtorweihen, S. J. *Chem. Theory Comput.* **2015**, *11*, 2329.
- (29) Marrink, S. J.; Tieleman, D. P.; Mark, A. E. *J. Phys. Chem. B* **2000**, *104*, 12165.
- (30) Hassan, N.; Ruso, J. M.; Piñeiro, Á. *Langmuir* **2011**, *27*, 9719.
- (31) Jorge, M. *Langmuir* **2008**, *24*, 5714.
- (32) Sammalkorpi, M.; Sanders, S.; Panagiotopoulos, A. Z.; Karttunen, M.; Haataja, M. *J. Phys. Chem. B* **2011**, *115*, 1403.
- (33) Nevidimov, A. V.; Razumov, V. F. *Mol. Phys.* **2009**, *107*, 2169.
- (34) Bond, P. J.; Sansom, M. S. P. *J. Am. Chem. Soc.* **2006**, *128*, 2697.
- (35) Velinova, M.; Sengupta, D.; Tadjer, A. V.; Marrink, S.-J. *Langmuir* **2011**, *27*, 14071.
- (36) Li, Z.; Wang, P.; Liu, B.; Wang, Y.; Zhang, J.; Yan, Y.; Ma, Y. *Soft Matter* **2014**, *10*, 8758.
- (37) Wallace, E. J.; Sansom, M. S. P. *Nanotechnology* **2009**, *20*, 045101.
- (38) Kirkensgaard, J. J. K.; Pedersen, M. C.; Hyde, S. T. *Soft Matter* **2014**, *10*, 7182.
- (39) Peter, C.; Kremer, K. *Soft Matter* **2009**, *5*, 4357.
- (40) Peter, C.; Kremer, K. *Faraday Discuss.* **2010**, *144*, 9.
- (41) Tschöp, W.; Kremer, K.; Hahn, O.; Batoulis, J.; Bürger, T. *Acta Polym.* **1998**, *49*, 75.
- (42) Tschöp, W.; Kremer, K.; Batoulis, J.; Bürger, T.; Hahn, O. *Acta Polym.* **1998**, *49*, 61.
- (43) Müller-Plathe, F. *Soft Mater.* **2002**, *1*, 1.
- (44) Santangelo, G.; Di Matteo, A.; Müller-Plathe, F.; Milano, G. *J. Phys. Chem. B* **2007**, *111*, 2765.
- (45) Spyriouni, T.; Tzoumanekas, C.; Theodorou, D.; Müller-Plathe, F.; Milano, G. *Macromolecules* **2007**, *40*, 3876.
- (46) Brasiello, A.; Russo, L.; Siettos, C.; Milano, G.; Crescitelli, S. *Comput.-Aided Chem. Eng.* **2010**, *28*, 62510.1016/S1570-7946(10)28105-1.
- (47) Shi, Q.; Voth, G. A. *Biophys. J.* **2005**, *89*, 2385.
- (48) Brocos, P.; Mendoza-Espinosa, P.; Castillo, R.; Mas-Oliva, J.; Pineiro, A. *Soft Matter* **2012**, *8*, 9005.
- (49) Khalatur, P. G. In *Polymer Science: A Comprehensive Reference*; Matyjaszewski, K., Möller, M., Eds.; Elsevier: Amsterdam, 2012; p 417.
- (50) Langner, K. M.; Sevink, G. J. A. *Soft Matter* **2012**, *8*, 5102.
- (51) Daoulas, K. C.; Muller, M. *J. Chem. Phys.* **2006**, *125*, 184904.
- (52) Stoykovich, M. P.; Muller, M.; Kim, S. O.; Solak, H. H.; Edwards, E. W.; de Pablo, J. J.; Nealey, P. F. *Science* **2005**, *308*, 1442.
- (53) Ramírez-Hernández, A.; Suh, H. S.; Nealey, P. F.; de Pablo, J. J. *Macromolecules* **2014**, *47*, 3520.
- (54) De Nicola, A.; Hezaveh, S.; Zhao, Y.; Kawakatsu, T.; Roccatano, D.; Milano, G. *Phys. Chem. Chem. Phys.* **2014**, *16*, 5093.
- (55) Zhao, Y.; De Nicola, A.; Kawakatsu, T.; Milano, G. *J. Comput. Chem.* **2012**, *33*, 868.
- (56) Milano, G.; Kawakatsu, T.; De Nicola, A. *Phys. Biol.* **2013**, *10*, 045007.
- (57) De Nicola, A.; Milano, G.; Kawakatsu, T. *Macromol. Chem. Phys.* **2013**, *214*, 1940.
- (58) De Nicola, A.; Zhao, Y.; Kawakatsu, T.; Roccatano, D.; Milano, G. *J. Chem. Theory Comput.* **2011**, *7*, 2947.
- (59) De Nicola, A.; Kawakatsu, T.; Milano, G. *J. Chem. Theory Comput.* **2014**, *10*, 5651.
- (60) Milano, G.; Kawakatsu, T. *J. Chem. Phys.* **2010**, *133*, 214102.
- (61) Milano, G.; Kawakatsu, T. *J. Chem. Phys.* **2009**, *130*, 214106.
- (62) Daoulas, K. C.; Muller, M.; de Pablo, J. J.; Nealey, P. F.; Smith, G. D. *Soft Matter* **2006**, *2*, 573.
- (63) De Nicola, A.; Zhao, Y.; Kawakatsu, T.; Roccatano, D.; Milano, G. *Theor. Chem. Acc.* **2012**, *131*, 1167.
- (64) Sevink, G. J. A.; Charlaganov, M.; Fraaije, J. G. E. M. *Soft Matter* **2013**, *9*, 2816.
- (65) Sevink, G. J. A.; Zvelindovsky, A. V. *Macromolecules* **2005**, *38*, 7502.
- (66) Paradies, H. H. *J. Phys. Chem.* **1980**, *84*, 599.
- (67) Hirsch, J. E. *Phys. Rev. B: Condens. Matter Mater. Phys.* **1983**, *28*, 4059.
- (68) Milano, G.; Santangelo, G.; Ragone, F.; Cavallo, L.; Di Matteo, A. *J. Phys. Chem. C* **2011**, *115*, 15154.
- (69) Chen, X.; Carbone, P.; Santangelo, G.; Di Matteo, A.; Milano, G.; Muller-Plathe, F. *Phys. Chem. Chem. Phys.* **2009**, *11*, 1977.
- (70) Brasiello, A.; Crescitelli, S.; Milano, G. *Faraday Discuss.* **2012**, *158*, 479.
- (71) Glatter, O.; Kratky, O. *Small-Angle X-ray Scattering*; Academic Press: New York, 1982.
- (72) Brookes, E.; Demeler, B.; Rocco, M. *Macromol. Biosci.* **2010**, *10*, 746.
- (73) Brookes, E.; Perez, J.; Cardinali, B.; Profumo, A.; Vachette, P.; Rocco, M. *J. Appl. Crystallogr.* **2013**, *46*, 1823.
- (74) de la Torre, J. G.; Bloomfield, V. Q. *Rev. Biophys.* **1981**, *14*, 81.
- (75) Rai, N.; Nöllmann, M.; Spertino, B.; Tassara, G.; Byron, O.; Rocco, M. *Structure* **2005**, *13*, 723.
- (76) Brookes, E.; Demeler, B.; Rosano, C.; Rocco, M. *Eur. Biophys. J.* **2010**, *39*, 423.
- (77) Rocco, M.; Byron, O. *Eur. Biophys. J.* **2015**, *44*, 417–43110.1007/s00249-015-1042-9.
- (78) Kang, E.-H.; Mansfield, M. L.; Douglas, J. F. *Phys. Rev. E* **2004**, *69*, 031918.
- (79) Mansfield, M. L.; Douglas, J. F. *Phys. Rev. E* **2008**, *78*, 046712.
- (80) Brookes, E.; Rocco, M. In *Analytical Ultracentrifugation: Instrumentation, Software and Application*; Uchiyama, S., Arisaka, F., Stafford, W. F., III, Laue, T. M., Eds.; Springer: New York, 2015; Chapter 10, in press.
- (81) Andersen, H. C. *J. Chem. Phys.* **1980**, *72*, 2384.
- (82) Berendsen, H. J. C.; van der Spoel, D.; van Drunen, R. *Comput. Phys. Commun.* **1995**, *91*, 43.
- (83) Van der Spoel, D.; Lindahl, E.; Hess, B.; Groenhof, G.; Mark, A. E.; Berendsen, H. J. C. *J. Comput. Chem.* **2005**, *26*, 1701.
- (84) Berendsen, H. J. C.; Postma, J. P. M.; van Gunsteren, W. F.; DiNola, A.; Haak, J. R. *J. Chem. Phys.* **1984**, *81*, 3684.

- (85) Frenkel, D.; Smit, B. *Understanding Molecular Simulations. From Algorithm to Applications*; Academic Press: San Diego, CA, 2002.
- (86) Hess, B.; Bekker, H.; Berendsen, H. J. C.; Fraaije, J. G. E. M. *J. Comput. Chem.* **1997**, *18*, 1463.
- (87) Anand, U.; Jash, C.; Mukherjee, S. *J. Colloid Interface Sci.* **2011**, *364*, 400.
- (88) Denkova, P. S.; Lokere, L. V.; Verbruggen, I.; Willem, R. *J. Phys. Chem. B* **2008**, *112*, 10935.
- (89) Brown, W.; Rymden, R.; Van Stam, J.; Almgren, M.; Svensk, G. *J. Phys. Chem.* **1989**, *93*, 2512.
- (90) Birdi, K. S. In *Surfactants, Adsorption, Surface Spectroscopy and Disperse Systems*; Lindman, B., Olofsson, G., Stenius, P., Eds.; Surface-Active Agents, Vol. 70; Steinkopff: Darmstadt, Germany, 1985; p 23.
- (91) Ruiz, C. C.; Molina-Bolívar, J. A.; Aguiar, J.; MacIsaac, G.; Moroze, S.; Palepu, R. *Langmuir* **2001**, *17*, 6831.
- (92) Molina-Bolívar, J. A.; Aguiar, J.; Ruiz, C. C. *J. Phys. Chem. B* **2002**, *106*, 870.
- (93) Stubičar, N.; Matejaš, J.; Zipper, P.; Wilfing, R. In *Surfactants in Solution*; Mittal, K. L., Ed.; Springer: Boston, 1989; p 181.
- (94) Daura, X.; van Gunsteren, W. F.; Mark, A. E. *Proteins: Struct., Funct., Genet.* **1999**, *34*, 269.
- (95) Daura, X.; Gademann, K.; Jaun, B.; Seebach, D.; van Gunsteren, W. F.; Mark, A. E. *Angew. Chem., Int. Ed.* **1999**, *38*, 236.
- (96) Karpen, M. E.; Tobias, D. J.; Brooks, C. L. *Biochemistry* **1993**, *32*, 412.
- (97) Jose, B. J.; Bales, B. L.; Peric, M. *J. Phys. Chem. B* **2009**, *113*, 13257.
- (98) Daful, A. G.; Avalos, J. B.; Mackie, A. D. *Langmuir* **2012**, *28*, 3730.
- (99) Jódar-Reyes, A. B.; Leermakers, F. A. M. *J. Phys. Chem. B* **2006**, *110*, 6300.
- (100) May, S.; Ben-Shaul, A. *J. Phys. Chem. B* **2001**, *105*, 630.
- (101) Al-Anber, Z. A.; Bonet Avalos, J.; Mackie, A. D. *J. Chem. Phys.* **2005**, *122*, 104910.
- (102) Galatanu, A. N.; Chronakis, I. S.; Anghel, D. F.; Khan, A. *Langmuir* **2000**, *16*, 4922.
- (103) Sallen, L.; Oswald, P.; Géminard, J. C.; Malthête, J. *J. Phys. II* **1995**, *5*, 937.
- (104) Oswald, P.; Géminard, J. C.; Lejcek, L.; Sallen, L. *J. Phys. II* **1996**, *6*, 281.
- (105) Petrov, P. G.; Ahir, S. V.; Terentjev, E. M. *Langmuir* **2002**, *18*, 9133.